Cell-free massive MIMO Channels in an Urban Environment - Measurements and Channel Statistics

Yuning Zhang, Thomas Choi, Zihang Cheng, Jorge Gomez-Ponce, *Member, IEEE*, Issei Kanno, Masaaki Ito, and Andreas F. Molisch, *Fellow, IEEE*

Abstract—**Cell-free massive MIMO (CF-mMIMO), where each user equipment (UE) is connected to multiple access points (APs), is emerging as an important component for 5G and 6G cellular systems. Accurate channel models based on measurements are required to optimize their design and deployment. This paper presents an extensive measurement campaign for CF-mMIMO in an urban environment. A new "virtual AP" technique measures channels between 80 UE locations and more than 20,000 possible microcellular AP locations. Measurements are done at 3.5 GHz carrier frequency with 350 MHz bandwidth (BW). The paper describes the measurement setup and data processing, shows sample results and their physical interpretation, and provides statistics for key quantities such as pathloss, shadowing, delay spread (DS), and delay window. We find pathloss coefficients of 2.9 and 10.4 for line-of-sight (LOS) and non line-of-sight (NLOS), respectively, where the high LOS coefficient is mainly because larger distance leads to more grazing angle of incidence and thus lower antenna gain in our setup. Shadowing standard deviations are 5.1/16.6 dB, and root mean squared (RMS) DSs of −80.6/ − 72.6 dBs. The measurements can also be used for parameterizing a CUNEC-type model, which will be reported in future work.**

Index Terms—**Cell-free Massive MIMO, Channel Sounding, Delay Dispersion, Delay Evolution, Urban Scenario**

I. INTRODUCTION

The progression from fourth-generation (4G) cellular systems to 5G and beyond is motivated by the requirements to increase the data rates and the reliability and uniformity of data services [2]. An especially promising architecture to achieve these goals is CF-mMIMO, which distributes in a geographical area a large number of base station (BS) antennas in the form of single-antenna (or few-antennas) APs, all of which are connected to a central processing unit via fast front haul connections [3], [4], [5, Chapter 22]. Each UE may connect wirelessly either to all APs or a subset encompassing the APs that are closest to it. This architecture provides more stable receive power than BSs with concentrated massive arrays since any UE is close to at least one AP. Furthermore, it eliminates

inter-cell interference because there are no cells anymore.[1] Thus, a CF-mMIMO system outperforms small-cell systems in particular in terms of 95%-likely per-user throughput and offers more robustness compared to conventional cellular systems [6], [7].

It is axiomatic that a good design of a wireless system must take into account the properties of the propagation channels in which the system will operate. The distributed nature of CF-mMIMO systems requires, therefore, channel models that correctly describe the interrelations between the propagation channels *from multiple UEs to multiple APs*. This is in contrast to the vast majority of current channel models (see also Sec. I-A) that consider the link between one or more UEs to a *single* BS. Obviously, such new models need to be based on new types of measurements.

A. State of the art

In contrast to the huge number of channel measurements performed with concentrated-MIMO setups, the number of *measurements* in CF-mMIMO systems is very small. Measurements generally fall into two categories: (i) outdoor measurements, which are characterized by a small number of APs, and (ii) indoor measurements, which often use virtual arrays for measurement and are easy to set up there.

In the former category, [8] focused on the measurement of capacity enhancement with four cooperating BSs that were all placed on walls surrounding a single courtyard; measurements were done at 5.2 GHz. Ref. [9] measured with a 3×2 system over a larger area, but in the 300 MHz range, while [10] measured the channel from UEs to two BSs at 73 GHz. Another type of outdoor measurement involves the movement of the UE. [11] investigated the downlink between 3 APs and a moving UE at 28 GHz, with only LOS channels. [12] and [13] measure at lower frequencies, namely at 5.9 GHz and 3.2 GHz, with 8 and up to 32 APs, respectively. While these measurements were important for the early development of CoMP, they do not involve a sufficient number of APs to allow modeling that is suitable for current CF-mMIMO systems. Specifically, deployment planning and system optimization requires measuring at *all potential* AP locations instead of only at a few locations with inter-AP distance separation, which in turn requires a much larger number of involved APs.

---

[1]CF-mMIMO is strongly related to the previously introduced concepts of base station cooperation, network MIMO, cooperative multipoint (CoMP), and Cloud-RAN.

In the indoor category, Ref. [14] measured an 8×8 virtual setup at 2.53 GHz in various rooms; [15] measured with a 64×64 array in a single room at 3.5 GHz, while [16] measured 8×8, but at 28 GHz. [17] measured at 3.5 GHz with a 7×7 setup in various indoor environments, but only the APs were distributed, while the 7 UE antennas were concentrated on a single device. [18] also measured at 3.5 GHz, with 64 different AP locations in an indoor corridor environment. Both [19] and [20] measured only in a single small room, but the former one measured at 2, 18, and 28 GHz, and the latter reference measured at 2.6 GHz with narrow BW. While these measurements are interesting, they are by definition not applicable to the main deployment case of CF-mMIMO, namely outdoor.

Large virtual outdoor setups were for the first time realized by the authors in [21], which suggested using a drone to fly a transmitter (Tx) to a number of different possible AP locations and measure there. The measurements achieved with this setup were used, e.g., in [22] to assess the energy efficiency of CF-mMIMO systems, and in [23] to develop a new street-by-street pathloss model called CUNEC. However, these measurements were limited in two aspects: (i) the available control of the drone limited the precision of the locations at which the virtual APs could be placed, and (ii) weight constraints required the use of a Tx with relatively narrow BW and poor phase stability.

B. Contribution of the paper

The current paper presents a measurement campaign that overcomes these limitations and provides the by far most extensive wideband measurements for CF-mMIMO channels, using 80 UE locations and a total of more than $20,000$ AP locations that are precisely tracked. The measurements are performed with 350 MHz BW. In particular, we

- describe a modification of our previous virtual array method that is better suited for wideband precision measurements.
- present sample results of the measurements, together with the interpretation of the observed evolutions of impulse responses in terms of the environment geometry.
- provide the statistics of pathloss, shadowing, and DS from this extensive measurement.

C. Paper organization

The rest of the paper is organized as follows: the measurement principle, the details of the channel sounder, and the measurement environment are described in Sec. II. This is followed in Sec. III by a description of the data processing and extraction method for the desired channel parameters. Sec. IV presents the sample results, while Sec. V presents the statistics of pathloss, shadowing, and delay dispersion. A summary concludes the paper in Sec. VI.

II. CHANNEL SOUNDING SYSTEM

Our measurements were performed with a very large MIMO array, where the AP side has a virtual array, created by mechanical movement of a single antenna along a trajectory,

effected by a "cherry-picker" vehicle that raises the Tx to a height of 13 m, i.e., a typical AP height. The UE side consists of an 8-element distributed switched array that remains static. The sounding of each single-input single-output (SISO) link within this array is done through a wideband multi-tone waveform. The following sections describe the various components of this setup in detail.

A. Channel Sounder

A photo of the complete setup can be seen in Fig. 1. Note that both the sounder equipment itself and the battery required to power it are much too heavy for mounting on a drone in the manner of the setup of [21].
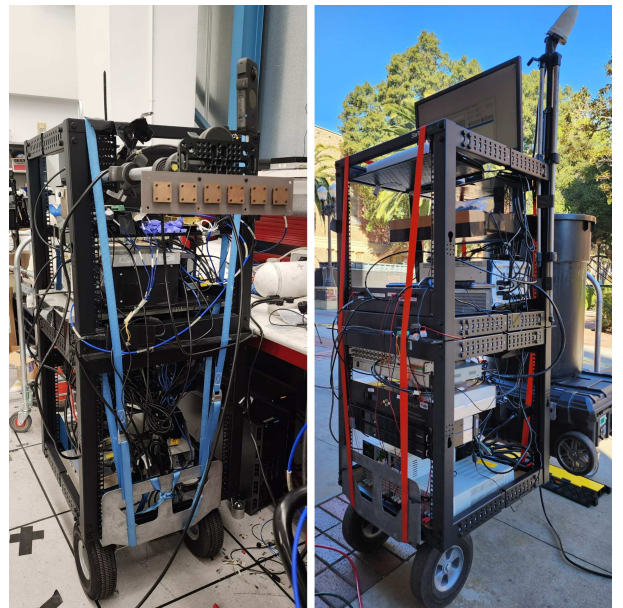

Fig. 1: Photo of the Tx and the Rx.

1) Transmitter: An arbitrary waveform generator (AWG), model Keysight N8241A, generates a sounding waveform with 350 MHz BW at an IF frequency of 375 MHz. Such generation at digital IF has the advantage that no IQ mixers are required for upconversion, which would, by definition, be more prone to create distortions by IQ imbalances. This signal is mixed with a 3.875 GHz sinusoidal oscillation from a precision frequency synthesizer (Eravant SOT-02220313200-SF-B6) to provide an RF signal with the center frequency of 3.5 GHz. Two concatenated band-pass filters (BPFs) (Pasternack PE8713) are used to suppress the local oscillator (LO) leakage and the upper sideband, and send the signal to two concatenated power amplifiers (PAs) (Wenteq ABP1500-03-3730 and Mini-Circuits ZHL-100W-382+, with amplification of 37 dB and 47 dB, respectively), providing an output power level of 42 dBm. The output is transmitted from a patch antenna element with vertical polarization (azimuth and elevation cuts, measured in our anechoic chamber with a standard gain horn, are shown in Fig. 2). A patch antenna was chosen as it can be expected to be the most prevalent antenna for CF-mMIMO APs, which are

typically mounted on house walls.[2] During the measurements, the array was mechanically down-tilted at an angle of $40-50°$, depending on the specific site location, to better align the main (vertical) transmission direction with the direction under which the UE is seen.
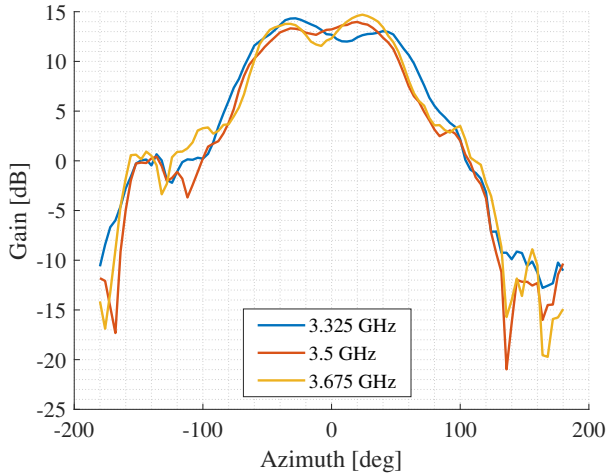
(a) Azimuth cut at 90° elevation
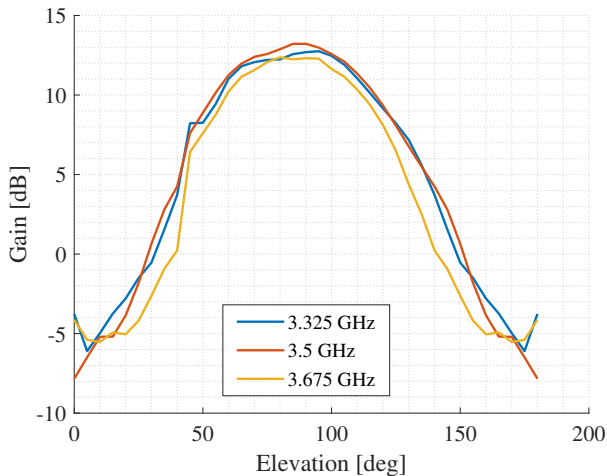
(b) Elevation cut at 0° azimuth

Fig. 2: Azimuth and elevation cut of the pattern of the patch antenna.

As a sounding sequence, we use a multi-carrier signal; it is similar to a Zadoff-Chu sequence used in LTE and 5G new radio (NR), but maintains a lower peak-to-average power ratio (PAPR) after filtering and over-sampling [24]–[27]. Within the 350 MHz BW (resulting in a delay resolution of 2.857 ns (0.857 m)), the waveform has $N_f = 2801$ subcarriers, resulting in a subcarrier spacing of $\Delta_f = 125$ kHz, corresponding to a maximum non-aliasing excess delay of 8 μs

(2400 m). The waveform has a duration of $T_{\mathrm{wfm}} = 8$ μs. Bursts of 10 repetitions of this waveform were transmitted for each location, which allows for improvement of the signal-to-noise ratio (SNR) in post-processing (see Sec. III).

2) Receiver: The receiver (Rx) antennas are 8 dipole antennas, with a nominally omni-directional pattern in the horizontal plane. Measurements of each of the patterns in our chamber showed variations with a standard deviation of 1.6 dB in azimuth; we consequently marked the "gain maximum" direction for each antenna and ensured in our deployment that they always pointed in the same direction along the street, to obtain uniformity/reproducibility of the gain.[3] Each of the antennas is connected to a low-noise amplifier (LNA) (Mini-Circuits ZX60-53LN+ with amplification of 20 dB and noise figure of 1.5 dB) to compensate for the attenuation of the subsequent long (30 m) RF cables. The long cables enable distributing the UEs over a 60 m large area, which is a requirement for our desired measurements (see also Sec. II-C). The cables are connected to an 8-to-1 switch (Pulsar SP8T, operating frequency range up to 12 GHz), whose output connects to a customized automatic gain control (AGC) unit. This unit consists of two digitally controllable attenuators, one with attenuation switchable between 0 and 30 dB and one with continuously adjustable attenuation between 0 and 120 dB with a resolution of 0.05 dB). Between these attenuators, two amplifiers of a total 59 dB amplification are placed. This arrangement keeps the power variations of its output within 1.2 dB standard deviation,[4] though the noise figure of the total setup can vary by up to 20 dB (the high noise figure occurs in the case of high received power so that the minimum (over the different locations) of the dynamic range is not limited by this). The output of the AGC is then mixed in a Mini-Circuits ZEM-4300MH+ mixer with an LO (same as for the Tx) for down-conversion to intermediate frequency (IF). This signal is then digitized by a National Instruments digitizer, PXIe-5162.

3) Synchronization and location recording: The system requires accurate synchronization for both switching control, carrier frequency, and sampling processes. This is achieved via two GPS-disciplined Rubidium (Rb) clocks (Jackson Labs HD CSAC 10 MHz at the Tx and Precision Test Systems GPS10eR at the Rx). To achieve best accuracy, those clocks need to be trained beforehand; we did this by a combination of 12-hour training inside our lab (where a GPS signal from a rooftop antenna is fed, via a cable, to the clocks), followed by another one-hour training when the equipment is outdoors to maintain the GPS tracking status and correct for inaccuracies arising during the short time between the clocks being disconnected from the GPS-carrying cables and the time the clocks are brought to an outdoor location where they have sufficient direct view of GPS satellites.

---

[2]Actually, the output of the PA is sent to a 1-to-8 high-power rated electronically-controlled RF switch follows after the PAs, which outputs to a uniform linear array (ULA) that contains four dual-ports (horizontally and vertically polarized, respectively) antenna elements and two dummy elements on each end. An NI controller yields a timed sequence to the switch. The four active antenna elements are switched one after the other, and the horizontal port is always the first one to be selected for each antenna element. Note, however, that in the current measurement campaign, only the signal from the first (vertically) polarized antenna element was used.

[3]While precision dipoles with guaranteed uniformity are commercially available and would have been preferable, obtaining 8 of them was cost-prohibitive.

[4]Strictly speaking, the AGC keeps the maximum of the power in the 8 Rx branches approximately constant, while the power of the other antennas can fluctuate more. The standard deviation for the strongest antenna is 1.2 dB over the part of the trajectory with LOS or strong NLOS, and 4.5 dB over the whole trajectory.

The clocks provide a 10 MHz reference and a 1 pulse per second (PPS) signal. The 10 MHz is used as a reference frequency/timing for all equipment, and the 1 PPS is aligned to UTC and is the start trigger for both the switches and the transceivers, i.e., the AWG and the digitizer.[5] The Tx switches every 80 μs after a SISO is captured, corresponding to 10 repetitions of waveforms.

The Rx switches every 640 μs, thus requiring 5.12 ms for a full Rx switching cycle (only the first 80μs provide useful signal, as discussed in footnote 2). The system then goes idle while transferring the MIMO snapshot data from the host memory to an external hard drive. A full Rx switching cycle occurs every 100 ms.

Since measurements are done with a virtual array, possible environment changes during the measurements need to be observed (and, if necessary, corresponding measurement points must be omitted). Thus, we mounted 360° cameras at each sounder and recorded at both Tx and Rx throughout the entire measurement campaign. Caution tapes are also used to prevent pedestrians from getting too close to the Rx antennas and blocking them.

The Tx was mounted in the basket of a cherry picker lift that is capable of driving with a raised basket; for safety reasons, a professional driver was used to operate the device. The driving speed was $0.4 - 0.6$ m/s, resulting in a spacing of the virtual array elements of $0.04 - 0.06$ m. Table I summarizes the most important measurement parameters.

We stress again that while the creation of virtual arrays by UEs on the ground is a common technique for channel sounding, creating such a large, dense array of APs has, to our knowledge, not been done before.

TABLE I: Measurement parameters

Parameter	Value
AP movement speed	$0.4 - 0.6$ m/s
AP/UE height	13 m / 1 m
AP/UE closest horizontal distance	3 m
AP antenna element 3 dB beamwidth	100°
Post-processing SNR gain	10 dB
SISO duration	80 μs
SIMO duration	640 μs
MIMO duration	5.12 ms
MIMO burst rate	10 Hz

B. Calibration Procedure

Evaluation of the measurements requires calibration of the sounder. This occurs in two steps: (i) back-to-back (B2B) calibration, and (ii) antenna calibration. For the former, the output of the Tx switch is connected not to the ULA, but rather, via a suitable attenuator, to the Rx input (note that the Rx includes the cables and the switch). The Tx then sends its sounding sequence, and the Rx digitizes this signal, thus establishing the transfer function. Since both Tx and Rx have 8 antenna ports each, we have a set of 64 B2B calibrations.

In a separate step, we calibrated the frequency-dependent antenna gain characteristics of the Tx antenna, as well as of all the Rx antennas. This calibration was done in the anechoic chamber at University of Southern California (USC), with a precision rotor rotating the antenna in 4° (in azimuth) and 5° (in elevation) steps, while the other link end is a calibrated standard gain antenna, and a vector network analyzer (VNA) to measure at the different frequencies. For the Tx antennas, we measured 360° azimuth and $45-180°$ elevation, and calibrated both by themselves and in combination with the switch; while for the Rx antennas, 360° azimuth, and $0-180°$ elevation was measured.

C. Measurement Locations

Measurements were performed in an urban (but not metropolitan) area in downtown Los Angeles, CA, USA, namely the USC University Park Campus. The measured area encompasses two city blocks, which cover a square of about 200×200 m, see Fig. 3. It is characterized by medium-height buildings (typically $3 \sim 4$ floors) interspersed with alleys and plazas; the width of the streets is between 3 and 15 m, depending on the specific street location.

The AP moves on a trajectory that covers the outer streets once, where the AP drives on the "further side" (with respect to the encircled street blocks) of the street, with the Tx antenna broadside pointing "inwards" perpendicular to the driving direction. The middle street is covered twice, with the Tx on different sides of the street, and pointing into different directions.[6] The AP maintains 13 m height throughout the trajectory as a typical AP height [28] (denoted as the blue line in Fig. 3), except for certain locations where the AP has to be lowered to $4 \sim 5$ m to avoid collision with tree canopies (shown as the yellow line). The Rxs are placed in 10 clusters of 8 antenna each, where the antennas are distributed over a 60 m wide area, such that the spacing between two adjacent UEs is approximately 8 m. For each placement of a UE cluster, the cherry picker drives along the whole trajectory. Due to setup and measurement time, only 2-3 clusters could be measured each day, and the total measurements were extended (including break days) for two weeks. No significant changes in the environment (e.g., due to construction) occurred during this time.

The trajectories thus encompass both LOS and NLOS situations, where we define the latter as blockage of the LOS by a building. Furthermore, parts of the LOS portions of the route are obstructed by foliage, which we henceforth denote as obstructed line-of-sight (OLOS). The tree canopies typically start at 8 m above the ground and extend beyond the height of the AP.

D. Clock drift correction

The movement of the AP may lose the locking of GPS timing signals, pushing the Rb clocks at the Tx and Rx into free-running mode with increased phase drift. We performed

---

[5]As mentioned in Sec. II-A, the Tx switched between different antenna elements, but only the signal from the first Tx antenna element is used.

[6]The cherry picker changes directions in the middle of that street, going in reverse to change direction; this is indicated by the dashed part of the line in Fig. 3.
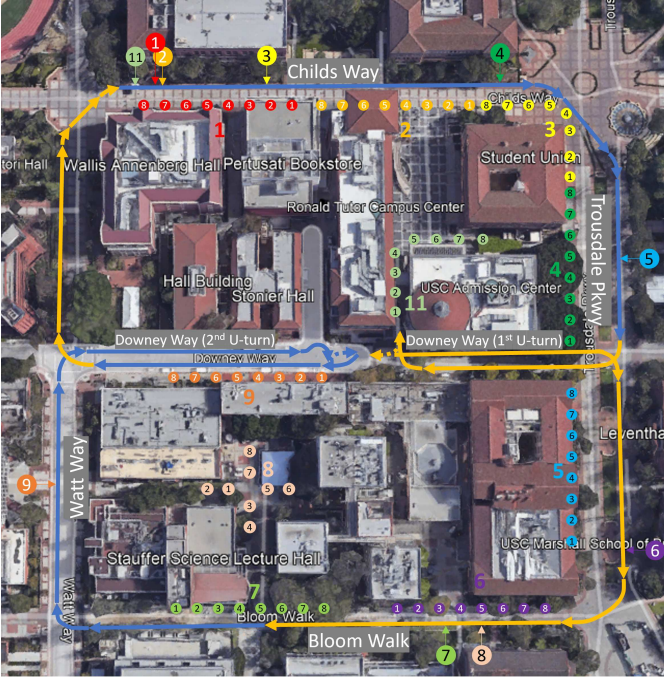
5

Fig. 3: Small colored dots: measurement UE site locations, each color represents one UE cluster. Large colored circle with an arrow: start/stop location of AP trajectory for a particular cluster.

a delay domain 2-stage correction based on the channel status. For LOS channels, we use the locations of APs and UEs acquired from the synchronized camera recordings from the real-time video recordings to compute the AP-UE distance as the true reference to compute the delay correction offset; for NLOS channels, we assume, based on the LOS measurements, that the phase drift is a linear function of time and compute the correction offset by linearly interpolating between the phases at the first/last LOS point next to a NLOS region. To estimate the residual error, we also perform a linear interpolation in the LOS region, and compare this interpolation against the true phase drift that we obtain as described above. The RMS error has an expected value of 0.43 m, and the standard deviation is 0.64 m. The CDF of the correlation distance of the error (i.e., the distance between two points such that the correlation between their distance offsets is $\frac{1}{e}$) from different LOS channels shows a mean value of 10m and for the 10% worst cases a correlation distance of 3 m, see Fig. 4. This indicates that the (unpredictable) deviations of the clock phase from the linear drift change relatively slowly.

III. DATA PROCESSING

This section describes the post-processing of the measured data to extract the channel impulse responses and condensed parameters derived from them.

A. Pre-processing of data

The received data are the temporal samples at the Rx, where each burst (Rx cycling through the Rx antennas, lasting
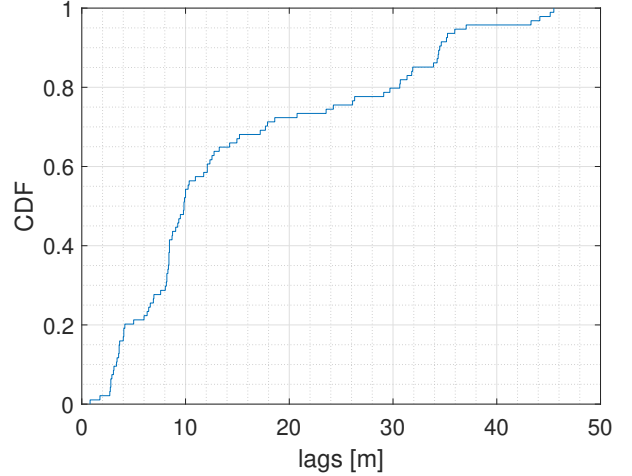

Fig. 4: CDF of the clockdrift decorrelation distance from all LOS channels

for 5.12 ms) is stored as a separate file named with the snapshot index (which can be related to the timestamps and thus locations in post-processing). We first perform a fast Fourier Transformation (FFT) over the captured time-domain data; since each such file represents a 10-times repetition of the sounding sequence, we then perform an averaging over those repetitions, resulting in a 10 dB SNR gain. We divide the result by the FFT of the sounding sequence, providing the "raw" transfer function of the channel $H_{\mathrm{raw},m,j,k}$, where m is the snapshot (time) index, j is the index of the Rx, and k is the frequency index.

From the digitizer (which has a sampling rate of 1.25 GS/s), we crop the 350 MHz IF band corresponding to the desired $3.325 - 3.675$ GHz passband. The cropped transfer function is then divided by the (cropped) B2B calibration transfer function $H_{\mathrm{cal},k}$. Note that the current measurements are not directionally resolved and all presented results contain the impact of both the channels and the antennas. Consequently, the transfer functions of both Tx and Rx antennas, which show some dependence on the considered direction (see, e.g., Fig. 2a), are contained in the transfer functions. The calibrated transfer function is then filtered with a Kaiser-Bessel filter with parameter $\beta = 3$ to reduce sidelobes in the delay domain. While the 3-dB BW is reduced by about a factor of 2 through this filtering, it is still larger than the typical band assignment for a 5G operator, i.e., 100 MHz. The transfer function is then furthermore zero-padded (extending the BW by a factor of 10), resulting in oversampling of the impulse response (its Fourier transform) as described below; this is important for accurate computation of the DS [29].

From the calibrated, cropped, filtered, zeroes-extended transfer function $H_{m,j,k}$, we then obtain the impulse response via Inverse Fast Fourier Transformation (IFFT), and from that the power-delay profile (PDP):

$$P_{\mathrm{h},m,j,\tau} = \left| \mathcal{F}_k^{-1} \{ H_{m,j,k} \} \right|^2 \tag{1}$$

where $\mathcal{F}^{-1}(\cdot)$ denotes the inverse Fourier transform with

respect to k, τ is the index in the Fourier dual domain (i.e., delay), and $\mathcal{F}^{-1}\{H_{m,j,i}(f)\}$ represents the complex CIR. We use here τ to denote any delay indexing scheme, irrespective of whether it is oversampled or not; the meaning is clear from the context. We then apply small-scale averaged (SSA) to all the PDPs using a sliding window with a width of 0.5 m (corresponding to 6 wavelengths). Note that this window length is a compromise between residual small-scale fading (SSF) and the need not to obscure actual changes in the SSA statistics; in particular, the delay-domain change of a multi-path component (MPC) within this window should be smaller than the resolvable delay bin.

We subsequently introduce thresholding at a level $\theta_{m',j}$ (on a dB scale) that is the maximum of a threshold $\theta_{n,m',j}$ that is Δ_n (set to 7 dB) above the average noise level $P_{n,m',j}$ of this SSF averaging window m', and a threshold that is Δ_{dr} (set to 20 dB) below the peak of the PDP in this window:

$$\theta_{m',j} = \max\left(P_{n,m',j} + \Delta_n, \ \max_{\tau}(P_{h,\tau}) - \Delta_{dr} \right) \quad (2)$$

We furthermore apply delay gating to the impulse response, such that all delay bins corresponding to a distance of > 343 m are set to zero. This was done since, in the considered geometry, no significant MPCs can be expected for longer delays. The combined operation of noise thresholding and delay gating can be written as [30]

$$P_h^{\mathrm{DG;NT}}(\tau) = \left[P_h(\tau) : (\tau \leq \tau_{\mathrm{gate}}) \cap (P_h(\tau) \geq \theta_{m',j}) \right] \quad (3)$$

A further important processing step is the elimination of impulse response precursors. In our measurements, we observed significant energy arriving *before* the LOS component (whose delay could be easily determined from the geometrical location of AP and UE). These precursors were not wraparound components (this could be excluded from the fact that such components would require a run length of more than 2 km). Rather, they are direct "talk through" from the Tx antenna into the Rx device, without the detour via the Rx antenna and cable. This explanation was confirmed by the fact that the precursors showed up at all UEs irrespective of their locations, and were furthermore exactly at the delay (which changed with Tx location) corresponding to the distance between the Tx antenna and the Rx sounder box. After having confirmed the source of the precursors, we could thus simply eliminate them in post-processing, i.e., all components arriving more than a "guard interval" (accommodating the Kaiser pulse corresponding to the LOS component) of 4 delay bins before the LOS component are set to zero. Note that this issue did not occur in NLOS situations, due to the large separation between Tx and Rx box.

B. Definition of parameters

1) Pathloss and shadowing: The path gain (PG), which is the inverse of the pathloss, is computed as

$$PG = \sum_{\tau} P_h(\tau) \quad (4)$$

For the PG we furthermore perform an averaging over a window of size 20 wavelength; such a larger window (com-

pared to the window used for eliminating the SSF in the PDP) is permissible here because MPCs moving from one resolvable delay bin to another is not a concern anymore; it has furthermore the advantage of better averaging out residual SSF fluctuations.

We will further use an $\alpha - \beta$ model to describe the pathloss as a function of distance between AP and UE:

$$PL_{\mathrm{dB}}(d) = \alpha \cdot 10 \log_{10}(d) + \beta + S \quad (5)$$

where α and β are the linear fitting coefficients, and S is a random variable describing shadowing; it is commonly assumed to be zero-mean Gaussian random variable (i.e., lognormal on a linear scale), and is characterized by its shadowing distribution. We will parameterize this model from our measurements because it is widely used for system simulations of CF-mMIMO [4]. However, it is worth noting that it does not reproduce important effects in urban microcells. The CUNEC model recently introduced by us [23] is better suited for such systems, but is more complex, so that its parameterization from our measurement campaign is left for future work.

We finally note that although the distance between APs can be non-uniform due to acceleration/deceleration of the cherry picker, the density changes are small. Thus, there is no need to perform a *weighted* pathloss model fitting as proposed in [31], [32].

2) Delay dispersion parameters: The DS is the most common condensed parameter for the description of the delay dispersion. It is defined as the second central moment of the PDP

$$\sigma_{\tau} = \sqrt{ \frac{\sum_{\tau} P_h(\tau)\tau^2}{\sum_{\tau} P_h(\tau)} - \left(\frac{\sum_{\tau} P_h(\tau)\tau}{\sum_{\tau} P_h(\tau)} \right)^2 } . \quad (6)$$

The DS depends significantly on the dynamic range. In order to avoid distortions of the statistics, we therefore only consider those PDP windows that have 20 dB dynamic range for the computation of the DS statistics.

While the DS is commonly used, it gives excessive weight to long-delayed MPCs. From a system design point of view, a better measure is the Q-window and the Q-tap number [5, Chapter 6]. Defining a threshold $\gamma = \frac{SIR_{\mathrm{ISI}}}{SIR_{\mathrm{ISI}}+1}$ (where SIR_{ISI} is the desired signal-to-intersymbol-interference ratio) the Q-window is defined as

$$Q_{\mathrm{win}} = \min_{x} x, \ s.t. \ \max_{T_0} \sum_{\tau=T_0}^{T_0+x} P_h(\tau) \geq \gamma PG. \quad (7)$$

We furthermore define the Q-tap number, using the *sorted* power in the resolvable delay bins $PDP_{\mathrm{sort}}(\tau_m)$ as:

$$Q_{\mathrm{tap}} = \min_{x} x, \ s.t. \ \sum_{m=1}^{x} PDP_{\mathrm{sort}}(\tau_m) \geq \gamma PG, \quad (8)$$

Q-window describes the length of an equalizer with contiguously-placed taps (or cyclic prefix in an OFDM system) that is necessary to achieve a certain SIR_{ISI}. Q-tap describes the number of taps in an equalizer (or Rake fingers in a Rake

receiver) that can place the taps at arbitrary delays.[7]

IV. SAMPLE PDPs

This section will describe sample measurement results and relate them to the geometry of the environment. It serves both to point out important propagation effects and as a sanity check for the measurements, supporting thus the total channel statistics that will be described in Sec. V. We note, however, that only delay information, and no angular information is available. Thus, we can verify whether propagation paths that are plausible (due to the mechanisms such as reflection at large buildings) are consistent with the observed delays,[8] but it is not possible to reconstruct with certainty the involved paths. Instead of using $\theta_{m',j}$ for parameter computation, all PDP examples presented in this section are processed with noise thresholding condition only, i.e., $P_{n,m',j} + \Delta_n$, to enable a richer presentation of propagation paths.

A. Snapshot of PDP

1) LoS PDP: Even in situations with relatively short distances between Tx and Rx, the PDP can exhibit surprising complexity, in particular in environments with inhomogeneous building structures. Fig. 5b shows an environment in which two UEs, namely Rx1 and Rx5 of the UE cluster 2 are placed at a location where a street opens into a plaza. The red triangle indicates the AP (raised into the air by the cherry picker), and the light gray triangle indicates the projection of the AP on the ground (the white dashed line between the two thus is a line perpendicular to the ground), while the green and orange hexagrams are locations of Rx1 and Rx5, respectively. From the geometry, we can conjecture various possible propagation paths, which are labeled with alphanumeric acronyms. Table III lists the potential paths and their corresponding delays, as well as the delays of peaks in the PDP that have similar delays. We can see that for Rx5, the AP and UE are very close, and not many propagation paths are feasible (most of those propagate "almost vertically"). Some of the conjectured paths are "nonspecular", by which we mean that the direction of incidence and direction of reflection do not follow Snell's law, or that the plane of reflection cannot be determined (as occurs, e.g., for foliage, but also for the cherry-picker, which has many metal parts pointed into different directions), see the PDP in Fig. 5a. Apart from the marked strong MPCs, the rest of the PDP shows a single-exponential decay. For Rx1, the multipath structure is richer, though the difference between the first and the second peak in the PDP is significantly larger. Most notable is that the PDP exhibits a second cluster, associated with MPCs that are reflected at the back of the plaza, and thus provide a strong reflection (note that on the day of the measurement, the umbrellas visible in the photo were closed). Such multiple clusters lead to a significant increase in both DS and Q-win.

---

[7]By length of an equalizer, we mean the length of the impulse response that the equalizer has to compensate. This may be different from the actual number of taps used in the linear filter that constitutes the equalizer [33].

[8]We further verified the potential propagation paths by comparing the evolution of their delay as to AP is moved to/from the location of the plotted PDP location, similar to the discussion in Sec. IV-B; for space reason these comparisons are not discussed further here.
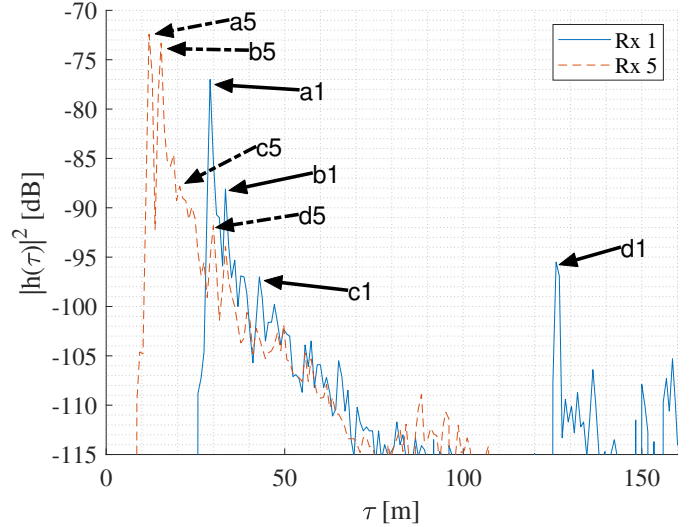
(a) Short LoS PDP

(b) The geometry map for the short LoS PDP

Fig. 5: LoS PDP sample where the AP is closer to the UE antennas. In b), the blue, red, green, and brown dash lines are paths $a5$, $b5$, $c5$, and $d5$.

2) NLoS PDP: Both the relative importance of propagation processes, and the shape of the PDP, show considerable differences to the LOS case. Direct propagation through the building can occur when the distance traversed through it is short, though the resulting MPC is considerably weaker than later-arriving components, leading to a "soft onset" of the PDP. Diffraction around the building, and over the rooftop, are both important factors, due to the shallow diffraction angle. In Fig. 6a, path $a1/b1$ is observable. However, it cannot be distinguished whether it is the in-building propagation, the horizontal diffraction around the square building, or the superposition of both because the two different paths share almost the same delay. Similarly, $a5$, $b5$, and $c5$ cannot be distinguished solely based on delay information. However, since the power at 90 m is weak, it can be concluded for all three possible paths, the propagation losses are all high.

TABLE II: Potential propagation MPCs and the corresponding routes for the short LoS sample

Path	Nominal Length	Actual Length	Explanation
a1	30.1	29.14	Direct path
b1	35	33.43	Building reflection/diffraction
c1	42.7	42.86	Tree reflection (**non-specular**)
d1	126.5	126	Building single reflection
a5	13	12	Direct path
b5	14.8	15.43	Building single reflection
c5	22	21.43	Building and the cherry picker double reflection (**non-specular**)
d5	30.5	30	Building/foliage double reflection (**non-specular**)

(a) NLoS PDP

(b) The geometry map for the NLoS PDP

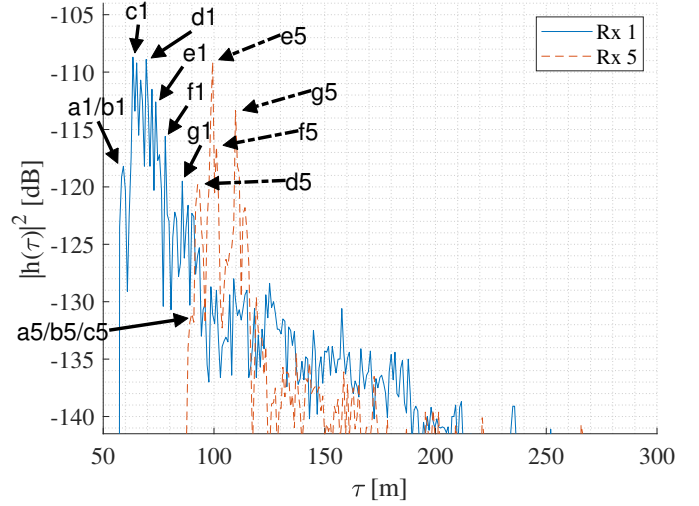Fig. 6: NLoS PDP sample around a corner of a street

One can also observe the reflection introduced by building walls and dense foliage by paths $d1$, $e1$, $g1$, $d5$, $e5$, $f5$, and $h5$. Particularly, we noticed a strong reflection from a copper statue at the lower right corner of Fig. 6b. The reason for $g5$ having lower path loss than $f1$ could be the shape of the statue, which provides a higher reflection cross section area for Rx5 compared to the one in direction of Rx1.

There are also a large number of MPCs at large delays, though we could not identify the specific propagation processes, as there are too many possible paths with multiple interactions that could explain them. When the separation between Tx and Rx is even larger, a smaller number of MPCs carry significant power, all caused by single-reflection processes. Table III summarizes the paths.

B. Evolution of PDP

A unique feature of our measurements is that we measure on trajectories of APs. It is thus desirable to analyze the evolution of the measured PDPs with locations (indicated by time) of the AP. This allows us to determine non-stationarities of the PDPs and have further sanity checks on the measurement results. These evolutions will also play a critical role in future CUNEC-type modeling for delay dispersion. Note that for space reasons, we discuss here only a smaller number of MPCs compared to the PDP snapshots.

The sample AP-location-dependent (AP-LD) PDP we discuss here is captured via a route shown in Fig. 7b, between the AP and Rx4 in the UE site 11. The color representation is now different from Fig. 3: the green part of the route now represents the LoS section, and the blue part is NLoS. The AP starts to move from the point at the upper right corner to the lower left of the map. The corresponding AP-LD PDP is shown in Fig. 7a. Due to the measurement principle of forming the virtual array, different AP locations map to different time, i.e., the *Time* axis in Fig. 7a. Rich scattering, i.e., many MPCs, can be observed throughout the trajectory. The first LOS situation occurs when the AP moves downward on the map and is in front of the plaza (similar to the AP location in Fig. 5). The
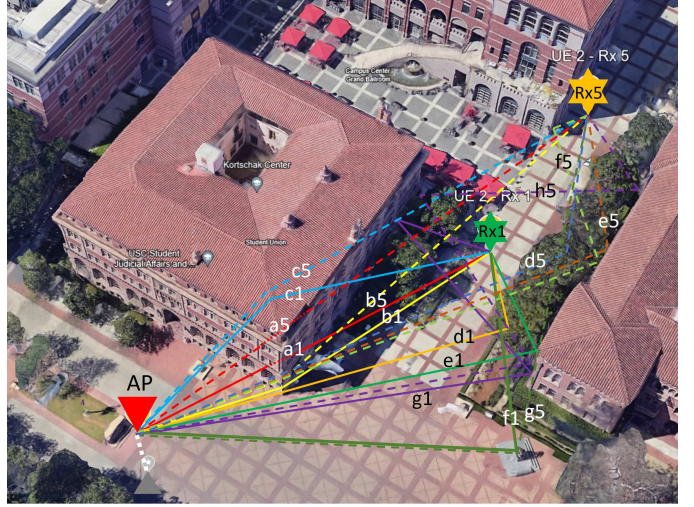
LOS a is the strongest component in this part of the PDP, lasting from approximate $t = 200$ to $t = 250$, and its delay increases as the AP moves further downwards. During the same time, the delay of MPCs b, which is reflected at the square building, decreases as the AP moves downwards, as the excess path length via this building becomes shorter. However, this component dies out sooner than the LOS, namely when the reflection on the building cannot fulfill Snell's laws anymore. For the subsequent 100s, there are no pronounced MPCs that could be ascribed to a particular propagation process, though there is still significant energy and an analysis of PDP snapshots (not shown here) reveals an essentially monotonic exponential decay. Around 350s, when the AP moves along the bottom horizontal trajectory, a gap between the building on the left and the Student Affairs building allows a low-attenuation channel, which is marked by c. While this is not strictly speaking a LOS, a reflection of the long rectangular building at the top of the map provides an efficient propagation path. When the AP approaches the bottom left point marked

TABLE III: Potential propagation MPCs and the corresponding routes for the NLoS sample

Path	Nominal Length	Actual Length	Explanation
a1	60.7	60.9	Direct link (through a building)
b1	60.9	60.9	Building edge diffraction
c1	65.1	65.1	Rooftop diffraction
d1	71.6	71.1	Foliage single reflection (**non-specular**)
e1	75.3	75.4	Building single reflection
f1	81	79.7	Trojan Tommy reflection
g1	87.6	87.4	Building double reflection
a5	90.8	90	Direct link (through building)
b5	91.5	90	Building edge diffraction
c5	91.1	90	Rooftop diffraction
d5	95	95.1	Foliage single reflection (**non-specular**)
e5	102.6	102	Building single reflection
f5	105.4	103.7	Building double reflection
g5	110.3	112.3	Trojan Tommy reflection
h5	134.8	NaN	Building triple reflection

(a) AP-LD PDP 1, the *Time* axis indicates the AP locations.

(b) Measurement route for AP-LD PDP 1. The green part of the trajectory is LOS, and the blue part is NLOS. Letters show the propagation effects giving rise to correspondingly labeled peaks in Fig. 7a.
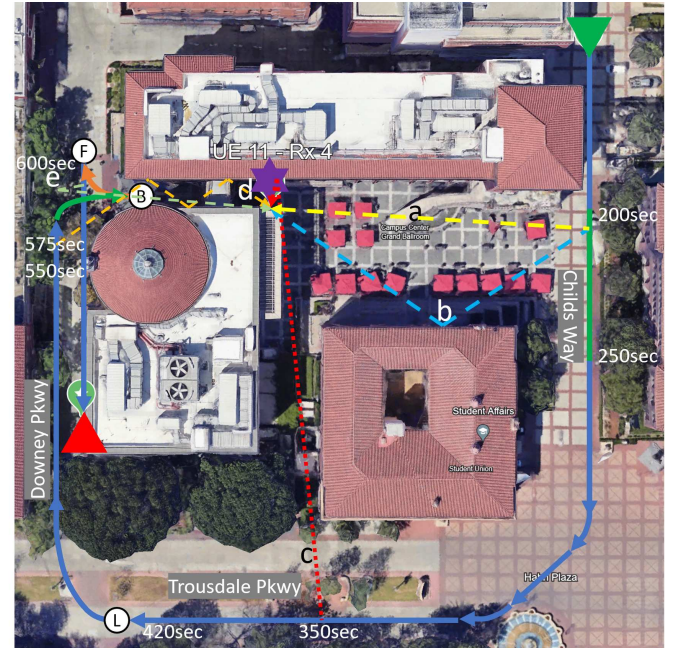
Fig. 7: AP-LD PDP at UE site 11, Rx 4

by a circled letter "L", the cherry picker lowers the AP to 3 m to avoid tree canopies when it goes into the "1st U-turn" street (the right half of Downey Way). Near 575s, the AP has LOS to the UE through the street canyon between the square buildings on the top and the left. Before it reaches this point, there are already multi-reflection components visible, such as d. The cherry picker then makes a U-turn at the location of the LOS visibility. The two circled letters "B" and "F" represent the driving mode of the cherry picker, which stands for "backward" and "forward" (the orange route represents the reverse route of the cherry picker), such that the orientation of the array changes. Note that (for the part of the trajectory on the left side of the map) the ULA is always facing to the right when the cherry picker is moving forward. Thus, when the cherry picker finishes the backward process, the ULA now faces to the left, which makes e happen: the LOS component is very weak, but the reflection of the opposing house wall is stronger.

Due to the variations of the noise figure mentioned in Sec. II-A, the noise floor is higher between time 550 sec and 600 sec, resulting in shorter support of the PDP after the noise thresholding.

Fig. 8 shows the pathloss and RMS DS evolution for the same scenario. While there is a general trend that high path gain and low DS occur together, there may be a significant deviation from this trend, e.g., at the end of the trajectory, where both path gain and DS decrease. This may be related to the location of the UE, i.e., between two close buildings. Such a narrow tunnel naturally filters out the MPCs with inappropriate incident directions (assuming specular reflections on building walls), and only the ones that share a similar propagation path from a certain direction can arrive at the UE, which makes the
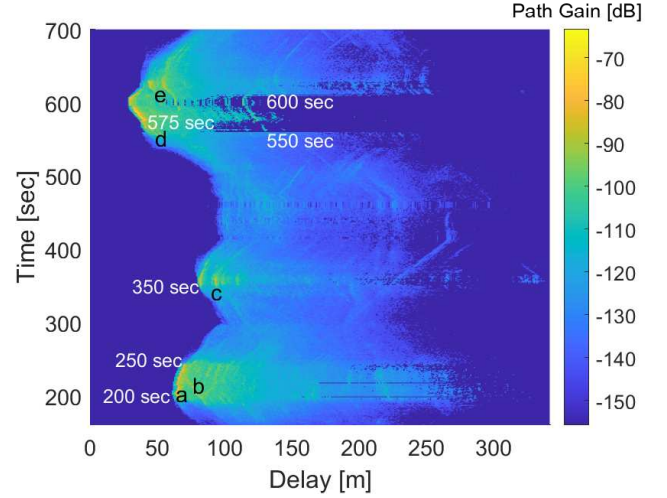
DS smaller. In the presence of LOS, the pathloss varies mostly within 5 dB when the distance does not change much, and the DS mostly is below -75 dBs. NLOS channels generally have both a higher DS and lower path gain, and a typically negative correlation between the two parameters.

Other examples of AP-location PDPs are provided in [1].

V. PARAMETER STATISTICS

We first describe the pathloss as a function of Euclidean distance. It must be kept in mind that this pathloss encompasses not only the actual attenuation by the channel, but is

TABLE IV: Pathloss and shadowing model parameters with 95% confidence interval.

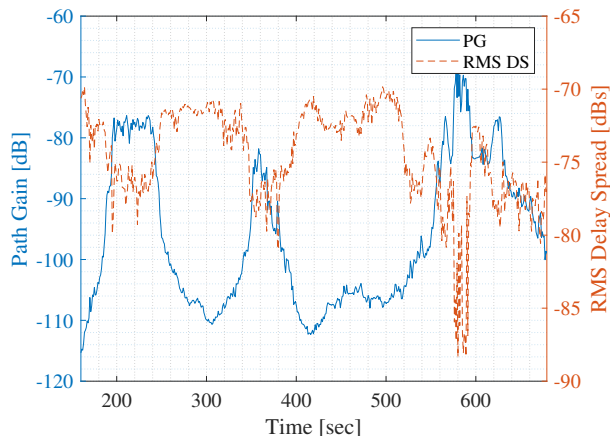| Parameter	Parameters estimated with 95% CI								
	α	$\alpha_{min,95\%}$	$\alpha_{max,95\%}$	β	$\beta_{min,95\%}$	$\beta_{max,95\%}$	σ_S	$\sigma_{S,min,95\%}$	$\sigma_{S,max,95\%}$
PL^{LoS}	2.95	2.95	2.95	34.42	34.31	34.53	5.14	5.13	5.15
PL^{NLoS}	10.37	10.36	10.39	-79.8	-80.16	-79.44	16.6	15.78	17.41

Fig. 8: Channel parameters evolving with different AP locations.

also influenced by the antenna pattern of both the Tx and Rx. This quantity is, by itself, meaningful when used for deployments with similar antennas; since patch antennas at the APs are common, and antennas with dipole-like radiation characteristics are also used frequently for UEs, indeed deployments "seeing" similar pathloss characteristics can be expected. However, the impact of the antenna patterns must be kept in mind when interpreting the results.

A. PL and Shadowing

A plot of the pathloss as a function of 3-D Euclidean distance for the ensemble of all UE-AP combinations is shown in Fig. 9a and 9b. Table IV shows the fitting parameters using the $\alpha - \beta$ model and the shadowing standard deviation. The distance ranges of the underlying measurements, and thus the validity range for the model, are $[12, 178]$ m and $[20, 262]$ m, for LOS and NLOS, respectively. We firstly note that the LOS pathloss shows a significantly higher standard deviation (around 5.1 dB) than is common in LOS scenarios. This is partly due to the large number of measurement points taken in a variety of streets that have different structures (surface structure of the buildings, number of plazas and alleys intersecting them, etc.). Furthermore, these streets contain different amounts of foliage that might obstruct the LOS MPC as well as other MPCs. Finally, the fits are significantly impacted by the antenna patterns, as discussed above. This is true in particular for LOS links, since in that case the pathloss will be heavily influenced by the antenna gains in the direction of the actual LOS MPC: when the AP is close to the UE, the LOS direction may be at elevation angles as large as $170°$ and thus - despite

the mechanical downtilt of the AP - antenna gains at both AP and UE might be very small, leading to a seeming increase in pathloss at small distances (we observed a similar effect in railway systems [34]). On the other hand, for large distances, the LOS MPC has a horizontally grazing angle of incidence at the AP antenna, leading to some additional attenuation. Thus, while LOS links in street canyons typically have $\alpha \leq 2$, in our case we find $\alpha = 2.95$.
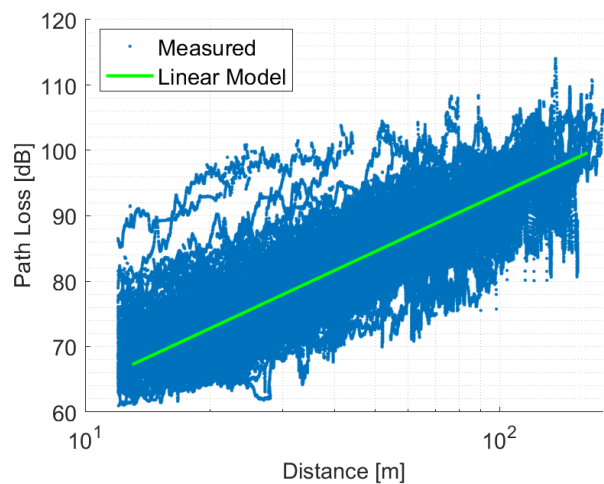
(a) LOS
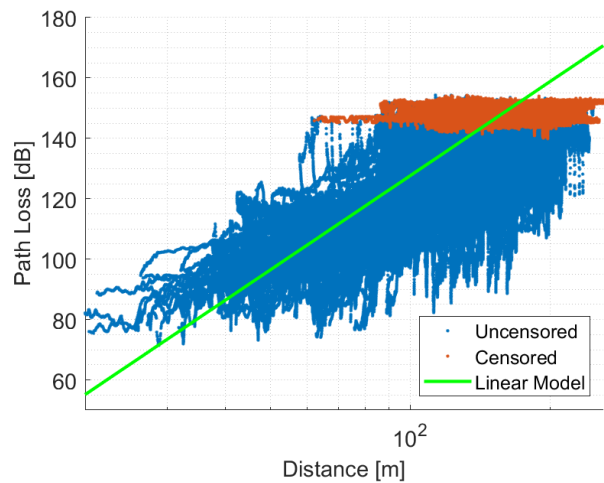
(b) NLOS

Fig. 9: Pathloss with linear model using logarithm distance. Bin-averaged with 5-m width.

To compute the linear regression in the LOS plot, we

TABLE V: RMS DS model parameters with 95% confidence interval.

Parameter	Statistical model parameters estimated with 95% CI					
	μ	$\mu_{min,95\%}$	$\mu_{max,95\%}$	σ	$\sigma_{min,95\%}$	$\sigma_{max,95\%}$
σ_τ^{LoS}	-80.6	-80.61	-80.58	3.67	3.66	3.68
$\sigma_\tau^{\text{NLoS}}$	-72.59	-72.6	-72.58	2.55	2.55	2.56

use a binning of the measured pathloss points into bins of width 2 m; this eliminates the impact of unequal number of measurement points at different distances (note that while the *spacing between* measurement points is essentially constant, the number of points at a given Euclidean distance from the UEs is different). Due to the height of the AP of 13 m and the UE of 1 m above ground, the minimum distance is 12 m (we eliminate measurements during the time that the cherry picker is at the ground level or in the process of lifting the basket from the ground level upwards, as those points do not correspond to typical AP deployments).

For the NLOS areas, there are locations where the received signal is censored (i.e., no signal power can be measured) because of the limitation of the system sensitivity. Our system sensitivity is defined by the noise threshold, namely $\theta_{m',j}$. Due to the nature of the dataset being the ensemble of all measurement campaigns, which spanned two weeks, with multiple system power cycles during transition and installation, a noise floor variation with a standard deviation of 1.3 dB can be observed. We perform the model fitting in the presence of censored data according to the method outlined in [35] and [36].

For the NLOS case, we find that the pathloss coefficient is than fir LOS, namely around 10.4. This leads to a mean pathloss around 84.51 vs 96.42 dB at 50 m and 98.58 vs 145.91 dB at 150 m distance, for LOS and NLOS, respectively. Higher attenuations exist, especially at even larger distances, but could not be measured due to the limited dynamic range of our setup.

B. Delay Spread

For the DS, we only consider those locations where at least 20 dB dynamic range is available in order not to bias the results. Taking the cumulative density function (CDF) of the DS separately for LOS and NLOS situations, we obtain Fig. 10 to show the measured distribution in our LOS and NLOS scenarios.

The distribution of the RMS DS is commonly modeled as a log-normal distribution, i.e., the DS in dBs is described by a normal distribution. We can see that the fits are good, with R^2 value of -0.0022 and -0.0245, respectively[9]. The fitting parameters are shown in Table V; median DS are on the order of -80.6 and -72.6 dBs, respectively. While this is small for an urban canyon environment, the microcellular setup (i.e., antennas below rooftop height) and thus the absence of far reflections explain the behavior.

[9]From the empirical data, a Log-Normal fit to the DS values on a dB scale provides a slightly better fit with parameter $R^2 = -0.0202$ dB for NLOS.
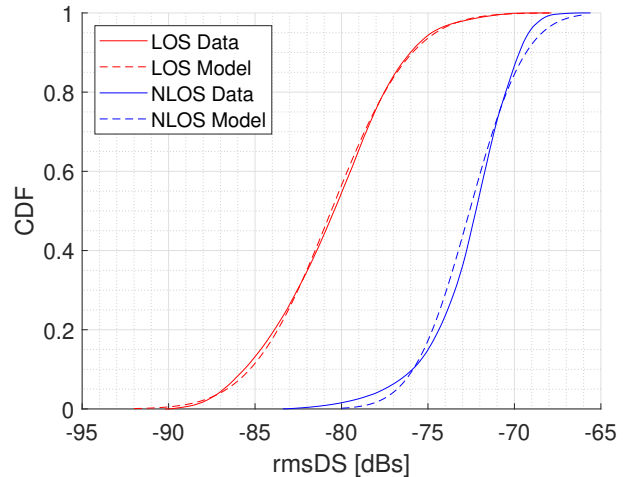

Fig. 10: RMS DS model that fits Gaussian distribution in the logarithm scale. For LOS: $R^2 = -0.0022$ dB; for NLOS: $R^2 = -0.0245$ dB.

Furthermore, we evaluated a linear fit of the DS as a function of AP-UE distance. Fig. 11a and 11b show the results for LOS and NLOS scenarios, respectively. We found the DS is almost independent of the distance (slope is -0.02) for LOS. We conjecture that this is due to the fact that the DS is mostly dominated by the immediate surroundings, such as the vicinity to plazas and street intersections, not the actual distance between AP and UE. As for the NLOS case, a negative slope of -0.33 occurs. This is somewhat in contrast to traditional models that describe the delay spread as increasing with distance. Again, we conjecture that this can be explained by the (sometimes significantly) below-rooftop position of the AP prevents the occurrence of long-delayed components that normally increase the DS for larger distances, and restricts the contributing MPCs to, essentially, waveguiding in the street canyon, and where the runlength differences between the guided components decrease as the distance increases.

C. Window parameters

Lastly, we analyze the distributions of the Q-win and Q-tap parameters, as defined and interpreted in Sec. III. They are expressed in units of resolvable delay bins (while for rectangular spectrum, this is usually assumed to be the inverse BW; the Kaiser filtering broadens it by a factor of 1.2). Naturally, these distributions show significant differences for LOS and NLOS situations, as shown in Fig. 12. Furthermore, they depend on the target SIR and the desired outage level (in the following, assumed to be 10%). For 10 dB, the Q-tap
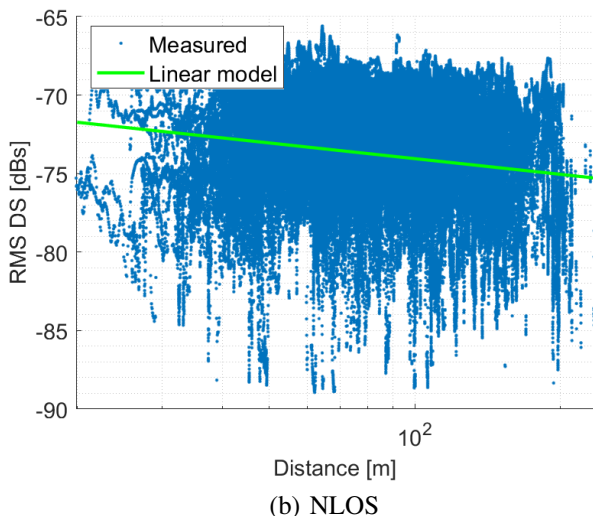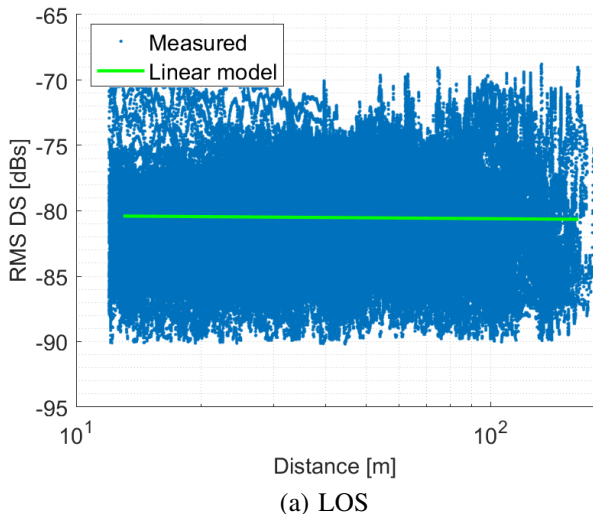
(a) LOS

(b) NLOS

Fig. 11: RMS DS with linear model using logarithm distance. Bin-averaged with 5-m width.

parameters are 12 and 69 and the Q-win parameters are 17 and 88 taps, for LOS and NLOS situations, respectively. The fact that Q-win and Q-tap differ from each other indicates that the PDPs show some sparsity. Non-negligible energy contributions at long-delayed MPCs need to be considered when designing the equalizers, rather than clustering closely.

VI. CONCLUSIONS

We have performed an extensive measurement campaign for determining the pathloss and delay dispersion of wideband CF-mMIMO channels. The dataset encompasses channels between more than $20,000$ AP locations and 80 UE locations, which is orders of magnitude larger than previous multi-BS outdoor measurements. After describing the measurement setup that is based on a combination of virtual and switched array, we presented sample results that explain the peaks in the measured PDPs in terms of the surrounding geometry and the specific propagation processes leading to each peak. Observations of
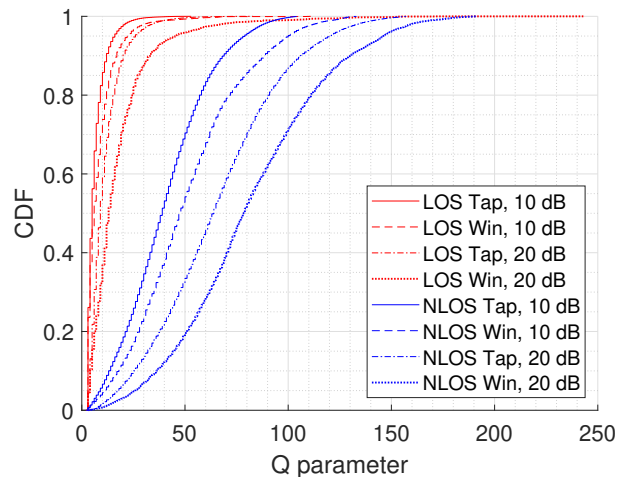

Fig. 12: Power distribution using quotient parameters, Q-tap and Q-window, with different required signal-to-interference ratios (SIRs)

the evolution of the MPCs from the plot of the PDP over time further confirm the measurement results and show the significant variations with the time/location of the APs. Finally, we extracted the statistics of the "classical" channel models, namely slope and intercept of the $\alpha - \beta$ model, shadowing standard deviation, DS, Q-win, and Q-tap.

The sample results give insights not only into the propagation channels, but also how CF-mMIMO systems would perform with different densities of APs, and number of APs belonging to one cluster. The differences in pathloss between LOS and NLOS are significant, namely up 50 dB (for the same distance AP-), indicating that deployment should be dense enough to guarantee that each UE has LOS to at least one AP. Obstruction of the LOS by vegetation is also a significant factor. At the same time, the strong difference between LOS and NLOS indicates that interference from nodes that have NLOS might be limited, which might enable smaller AP clusters connected to each UE. It is also remarkable that not only the channel transfer function, but also the PDP, and thus the frequency correlation function, can differ significantly for the links from one UE to different APs, which might complicate acquisition and exploitation of second-order channel statistics.

Finally, the traditional channel statistics such as $\alpha - \beta$ pathloss model and DS are valuable for system simulations when the underlying generic channel model is based on those specific quantities, as is the case in most theoretical investigations of CF-mMIMO systems. However, the experimental results in this paper confirm that there are significant variations between statistics of different streets, and that the long-term correlations must be taken into account on a per-street basis. Future work will thus focus on the development of a wideband channel model that can properly quantify these effects, generalizing our CUNEC approach that we previously introduced for the modeling of pathloss.

VII. ACKNOWLEDGMENT

References

[1] Y. Zhang, T. Choi, Z. Cheng, I. Kanno, M. Ito, J. Gomez-Ponce, H. Hammoud, B. Wu, A. Pradhan, K. Arana, P. Krishna, T. Yang, T. Chen, I. Vasishtha, H. Xie, L. Sun, and A. F. Molisch, "Large-scale outdoor cell-free mMIMO channel measurement in an urban scenario at 3.5 GHz," in *Submitted to 2024 IEEE 100th Vehicular Technology Conference (VTC-Fall)*. IEEE, 2024. [Online]. Available: https://arxiv.org/pdf/2405.20617

[2] H. Tataria, M. Shafi, A. F. Molisch, M. Dohler, H. Sjöland, and F. Tufvesson, "6G wireless systems: Vision, requirements, challenges, insights, and opportunities," *Proceedings of the IEEE*, vol. 109, no. 7, pp. 1166–1199, 2021.

[3] J. Zhang, S. Chen, Y. Lin, J. Zheng, B. Ai, and L. Hanzo, "Cell-free massive MIMO: A new next-generation paradigm," *IEEE Access*, vol. 7, pp. 99 878–99 888, 2019.

[4] Özlem Tugfe Demir, E. Björnson, and L. Sanguinetti, "Foundations of user-centric cell-free massive MIMO," *Found. and Trends Signal Process.*, vol. 14, no. 3-4, pp. 162–472, 2021.

[5] A. F. Molisch, *Wireless Communications - from fundamentals to beyond 5G*, 3rd ed. IEEE Press - Wiley, 2023.

[6] H. Q. Ngo, A. Ashikhmin, H. Yang, E. G. Larsson, and T. L. Marzetta, "Cell-free massive MIMO: Uniformly great service for everyone," in *2015 IEEE 16th international workshop on signal processing advances in wireless communications (SPAWC)*. IEEE, 2015, pp. 201–205.

[7] E. Nayebi, A. Ashikhmin, T. L. Marzetta, and H. Yang, "Cell-free massive MIMO systems," in *2015 49th Asilomar Conference on Signals, Systems and Computers*, 2015, pp. 695–699.

[8] V. Jungnickel, S. Jaeckel, L. Thiele, L. Jiang, U. Kruger, A. Brylka, and C. Von Helmolt, "Capacity measurements in a cooperative MIMO network," *IEEE transactions on vehicular technology*, vol. 58, no. 5, pp. 2392–2405, 2008.

[9] A. R. Hammons, J. R. Hampton, N. M. Merheb, and M. Cruz, "Cooperative MIMO field measurements for military UHF band in low-rise urban environment," in *2008 5th IEEE Sensor Array and Multichannel Signal Processing Workshop*. IEEE, 2008, pp. 122–126.

[10] G. R. MacCartney, T. S. Rappaport, and A. Ghosh, "Base station diversity propagation measurements at 73 GHz millimeter-wave for 5G coordinated multipoint (CoMP) analysis," in *2017 IEEE Globecom Workshops (GC Wkshps)*. IEEE, 2017, pp. 1–7.

[11] D. Kurita, K. Tateishi, A. Harada, Y. Kishiyama, S. Itoh, H. Murai, A. Simonsson, and P. Ökvist, "Outdoor experiments on 5G radio access using distributed MIMO and beamforming in 28-GHz frequency band," in *2017 IEEE 28th Annual International Symposium on Personal, Indoor, and Mobile Radio Communications (PIMRC)*, 2017, pp. 1–6.

[12] E. P. Simon, P. Laly, J. Farah, E. Tanghe, W. Joseph, and D. P. Gaillot, "Measurement of the V2I channel in cell-free vehicular networks with the distributed mamimosa channel sounder," in *2023 17th European Conference on Antennas and Propagation (EuCAP)*, 2023, pp. 1–5.

[13] D. Loschenbrand, M. Hofer, L. Bernado, S. Zelenbaba, and T. Zemen, "Towards cell-free massive MIMO: A measurement-based analysis," *IEEE Access*, vol. 10, p. 89232–89247, 2022. [Online]. Available: http://dx.doi.org/10.1109/ACCESS.2022.3200365

[14] I. Dey, P. S. Rossi, M. M. Butt, and N. Marchetti, "Virtual MIMO wireless sensor networks: Propagation measurements and fusion performance," *IEEE Transactions on Antennas and Propagation*, vol. 67, no. 8, pp. 5555–5568, 2019.

[15] T. Choi, P. Luo, A. Ramesh, and A. F. Molisch, "Co-located vs distributed vs semi-distributed MIMO: Measurement-based evaluation," in *2020 54th Asilomar Conference on Signals, Systems, and Computers*. IEEE, 2020, pp. 836–841.

[16] N. Tawa, T. Kuwabara, Y. Maruta, and T. Kaneko, "Measuring propagation channel variations and reciprocity using 28 GHz indoor distributed multi-user mimo," in *2020 IEEE Radio and Wireless Symposium (RWS)*. IEEE, 2020, pp. 104–107.

[17] Y. Zhang, L. Xiao, S. Zhou, J. Wang *et al.*, "Measurement-based spatial correlation and capacity of indoor distributed MIMO system," *International Journal of Antennas and Propagation*, vol. 2013, 2013.

[18] J. Pérez, O. Fernandez, L. Valle, A. Bedoui, M. Et-tolba, and R. Torres, "Experimental analysis of concentrated versus distributed massive MIMO in an indoor cell at 3.5 GHz," *Electronics*, vol. 10, p. 1646, 07 2021.

[19] R. J. Bultitude and M. Alkadamani, "Radio-propagation-measurement-based simulations of the capacity of multi-user D-MIMO indirect path communication systems in a small cluttered room at 2, 18, and 28 ghz," in *2017 IEEE 86th Vehicular Technology Conference (VTC-Fall)*. IEEE, 2017, pp. 1–5.

[20] C. Li, S. De Bast, E. Tanghe, S. Pollin, and W. Joseph, "Toward fine-grained indoor localization based on massive MIMO-OFDM system: Experiment and analysis," *IEEE Sensors Journal*, vol. 22, no. 6, pp. 5318–5328, 2022.

[21] T. Choi, J. Gomez-Ponce, C. Bullard, I. Kanno, M. Ito, T. Ohseki, K. Yamazaki, and A. F. Molisch, "Using a drone sounder to measure channels for cell-free massive MIMO systems," in *2022 IEEE Wireless Communications and Networking Conference (WCNC)*. IEEE, 2022, pp. 2506–2511.

[22] T. Choi, M. Ito, I. Kanno, T. Oseki, K. Yamazaki, and A. F. Molisch, "Uplink energy efficiency of cell-free massive MIMO with transmit power control in measured propagation channels," in *2021 IEEE Workshop on Signal Processing Systems (SiPS)*. IEEE, 2021, pp. 164–169.

[23] T. Choi, I. Kanno, M. Ito, W.-Y. Chen, and A. F. Molisch, "A realistic path loss model for cell-free massive MIMO in urban environments," in *GLOBECOM 2022-2022 IEEE Global Communications Conference*. IEEE, 2022, pp. 2468–2473.

[24] S. Boyd, "Multitone signals with low crest factor," *IEEE Transactions on Circuits and Systems*, vol. 33, no. 10, pp. 1018–1022, 1986.

[25] J.-M. Conrat, P. Pajusco, and J.-Y. Thiriet, "A multibands wideband propagation channel sounder from 2 to 60 GHz," in *2006 IEEE Instrumentation and Measurement Technology Conference Proceedings*, 2006, pp. 590–595.

[26] R. Wang, C. U. Bas, O. Renaudin, S. Sangodoyin, U. T. Virk, and A. F. Molisch, "A real-time MIMO channel sounder for vehicle-to-vehicle propagation channel at 5.9 GHz," in *2017 IEEE International Conference on Communications (ICC)*, 2017, pp. 1–6.

[27] C. U. Bas, R. Wang, S. Sangodoyin, D. Psychoudakis, T. Henige, R. Monroe, J. Park, C. J. Zhang, and A. F. Molisch, "Real-time millimeter-wave MIMO channel sounder for dynamic directional measurements," *IEEE Transactions on Vehicular Technology*, vol. 68, no. 9, pp. 8775–8789, 2019.

[28] 3GPP, "5G: Study on channel model for frequencies from 0.5 to 100 GHz," 3rd Generation Partnership Project (3GPP), Technical Specification (TS) 38.901, Version 14.0.0, 5 2017. [Online]. Available: https://www.etsi.org/deliver/etsi_tr/138900_138999/138901/14.00.00_60/tr_138901v140000p.pdf

[29] J. Gomez-Ponce, N. A. Abbasi, Z. Cheng, S. Abu-Surra, G. Xu, J. Zhang, and A. F. Molisch, "Impact of noisy measurements with fourier-based evaluation on condensed channel parameters," *IEEE Transactions on Wireless Communications*, 2023.

[30] N. A. Abbasi, J. L. Gomez, R. Kondaveti, S. M. Shaikbepari, S. Rao, S. Abu-Surra, G. Xu, J. Zhang, and A. F. Molisch, "THz band channel measurements and statistical modeling for urban D2D environments," *IEEE Transactions on Wireless Communications*, vol. 22, no. 3, pp. 1466–1479, 2023.

[31] A. Karttunen, A. F. Molisch, R. Wang, S. Hur, J. Zhang, and J. Park, "Distance dependence of path loss models with weighted fitting," in *2016 IEEE International Conference on Communications (ICC)*, 2016, pp. 1–6.

[32] J. G. Ponce, T. Choi, N. A. Abbasi, A. Adame, A. Alvarado, C. Bullard, R. Shen, F. Daneshgaran, H. S. Dhillon, and A. F. Molisch, "Air-to-ground directional channel sounder with 64-antenna dual-polarized cylindrical array," *IEEE Int. Conf. Comm. Workshops*, 2021.

[33] Proakis, *Digital Communications 5th Edition*. McGraw Hill, 2007.

[34] R. He, A. F. Molisch, Z. Zhong, B. Ai, J. Ding, R. Chen, and Z. Li, "Measurement based channel modeling with directional antennas for high-speed railways," in *2013 IEEE Wireless Communications and Networking Conference (WCNC)*. IEEE, 2013, pp. 2932–2936.

[35] C. Gustafson, T. Abbas, D. Bolin, and F. Tufvesson, "Statistical modeling and estimation of censored pathloss data," *IEEE Wireless Communication Letters*, 04 2015.

[36] A. Karttunen, C. Gustafson, A. F. Molisch, R. Wang, S. Hur, J. Zhang, and J. Park, "Path loss models with distance-dependent weighted fitting and estimation of censored path loss data," *IET Microwaves, Antennas & Propagation*, vol. 10, no. 14, pp. 1467–1474, 2016.